NANO LETTERS

pubs.acs.org/NanoLett
Letter

Nanoscale Magnetic Arrays through Block Copolymer Templating of Polyoxometalates

Daniel R. M. Clyde, David L. Cortie, Simon Granville, David C. Ware, Penelope J. Brothers, and Jenny Malmström*

Cite This: *Nano Lett.* 2024, 24, 2165−2174

ABSTRACT: Magnetic nanoarrays promise to enable new energy-efficient computations based on spintronics or magnonics. In this work, we present a block copolymer-assisted strategy for fabricating ordered magnetic nanostructures on silicon and permalloy substrates. Block copolymer micelle-like structures were used as a template in which polyoxometalate (POM) clusters could assemble in an opal-like structure. A combination of microscopy and scattering techniques was used to confirm the structural and organizational features of the fabricated materials. The magnetic properties of these materials were investigated by polarized neutron reflectometry, nuclear magnetic resonance, and magnetometry measurements. The data show that a magnetic structural design was achieved and that a thin layer of patterned POMs strongly influenced an underlying permalloy layer. This work demonstrates that the bottom-up pathway is a potentially viable method for patterning magnetic substrates on a sub-100 nm scale, toward the magnetic nanostructures needed for spintronic or magnonic crystal devices.

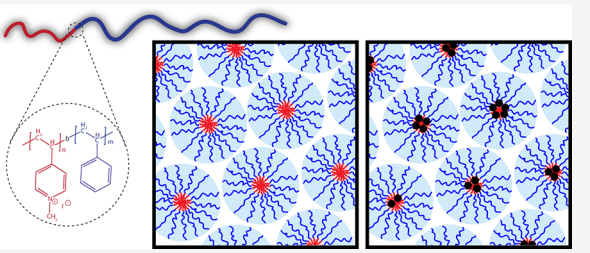

KEYWORDS: *exchange bias, block copolymer, polyoxometalate, magnon, polarized neutron reflectometry*

Current data storage technologies have limitations in storage capacity, density, lifetime, and in particular energy consumption.[1] The energy consumption is largely associated with cooling of waste heat generated through electron mobility and electrical resistance, which accounts for ∼40% of the energy consumed per data center.[2] In theory, spin-wave technologies have the potential to minimize the heat output from such systems, while also operating at higher frequencies, allowing for faster and more compact modern devices.[3,4]

Spin-waves, also known as magnons, are generated when a magnetic disturbance is introduced into a magnetically ordered material.[5] This disturbance propagates throughout the material, which in turn produces a detectable signal.[6] To transport magnons in a controlled manner, spin-wave guides are required as the signal carrier. Spin-waves are typically studied in thin films, and uniformly patterned structures in the submicrometer range are generally required to successfully manipulate spin-waves.[7,8] Such systems are called magnonic crystals and are conventionally fabricated via top-down approaches, which include thin film deposition, followed by patterning using lithography methods.[9−12] However, lithographic approaches are not well suited for fabricating structures for generating spin-waves with wavelengths of <100 nm, limiting the potential of fully realizing spin-wave propagation at terahertz frequencies.[13,14]

Block copolymers (BCPs) are well-known for being robust systems in terms of their ordering and patterning abilities, down to feature sizes of 5 nm.[15] The sizes and spacing of the structures are modulated by the polymer chain lengths. Block copolymers have been used extensively to organize nanoparticles in different schemes to form composite materials consisting of various nanoparticle/polymer systems[16−19] for applications in, for example, photonics,[20] photoluminescence,[21] spintronics,[22] and electrochromism.[23] Magnetic cargo can also be incorporated or grown within these well-ordered systems,[24−26] to make a wide range of magnetically patterned structures for magnonics.

One type of structurally and functionally diverse cargo that can be incorporated into block copolymers is polyoxometalates (POMs). POMs make up a class of inorganic compounds (in the nanometer size range) based on anionic metal oxides, which offer enormous structural and functional diversity.[27] POMs have found widespread use in the fields of magnetism, medicine, electrochemistry, optical sensing, and other materials science applications.[28−31] Accounting for these applications are

Received: October 17, 2023
Revised: February 1, 2024
Accepted: February 2, 2024
Published: February 8, 2024

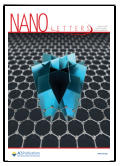

https://doi.org/10.1021/acs.nanolett.3c03825
Nano Lett. 2024, 24, 2165−2174

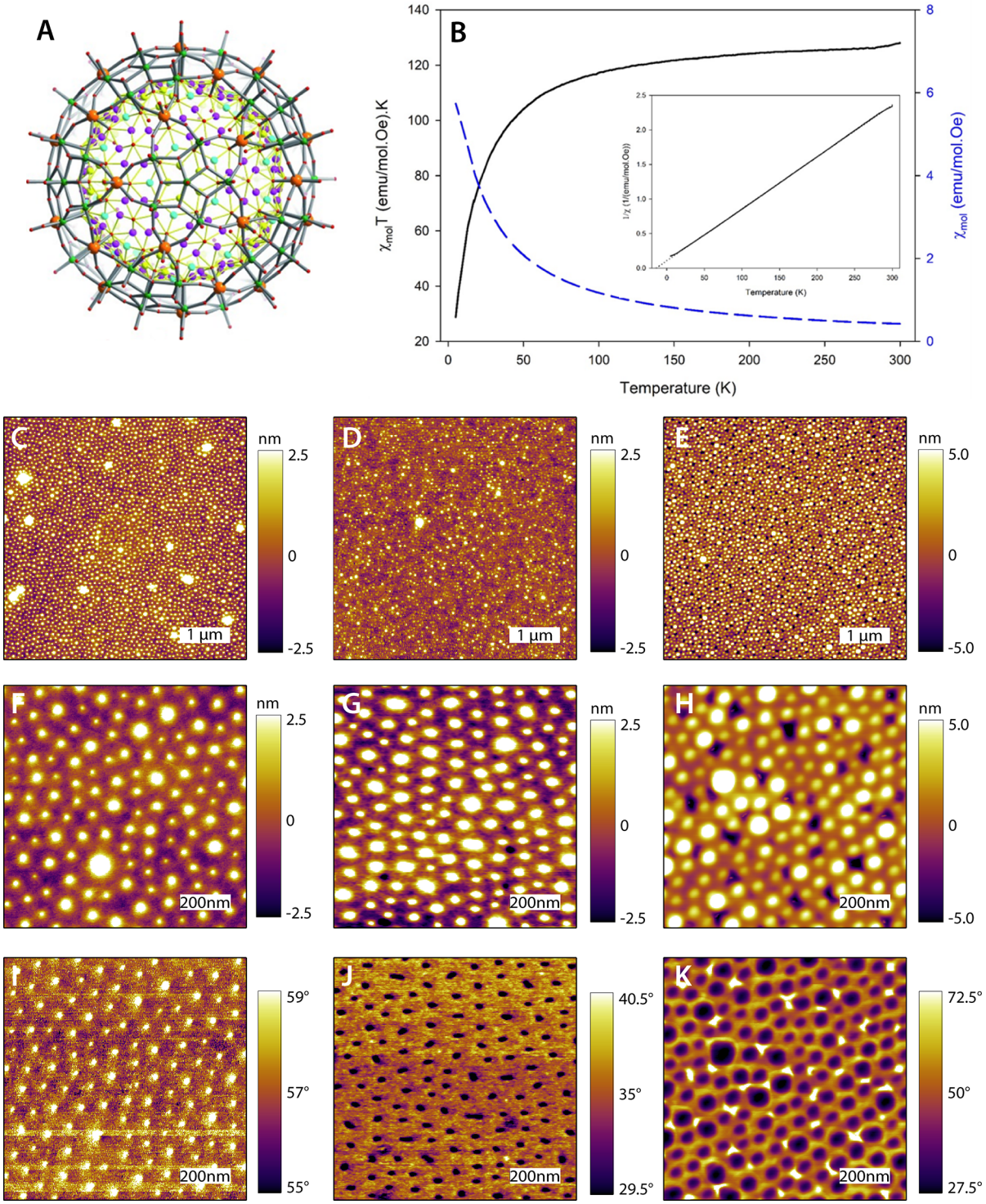

Figure 1. (A) Ball-and-stick representation of the $Fe_{30}W_{72}$ POM, excluding NH_4^+ ions: W in green, Fe in orange, O in red, S in yellow, turquoise, and lilac in the form of SO_4^{2-} ligands in various coordination environments. Reproduced with permission from ref 42. Copyright 2010 Wiley. (B) Temperature dependence of $\chi_{mol}T$ (black) and χ_{mol} (blue). The inset shows the temperature dependence of $1/\chi_{mol}$ for $Fe_{30}W_{72}$ measured at 1 T. The dotted regression line in the inset extends to the *x*-intercept identifying the Curie–Weiss temperature (θ) of −14 K. (C–H) Topographic images generated by AFM at different length scales and (I–K) phase images corresponding to the topography in panels F–H, respectively. The left column (C, F, and I) shows micelles only, as deposited. The central column (D, G, and J) shows the micelles after water exposure, while the right column (E, H, and K) shows the micelles after exposure to an $Fe_{30}W_{72}$ solution.

their relative stability under neutral and acidic conditions, clusters of transition metal centers, redox-active sites, and a large number of different spin states.[22] POMs have previously been deposited at interfaces through simple dip/drop coating methods, solvothermal deposition, and electrodeposition.[32] Several interesting substrate effects have been observed for

https://doi.org/10.1021/acs.nanolett.3c03825
Nano Lett. 2024, 24, 2165−2174

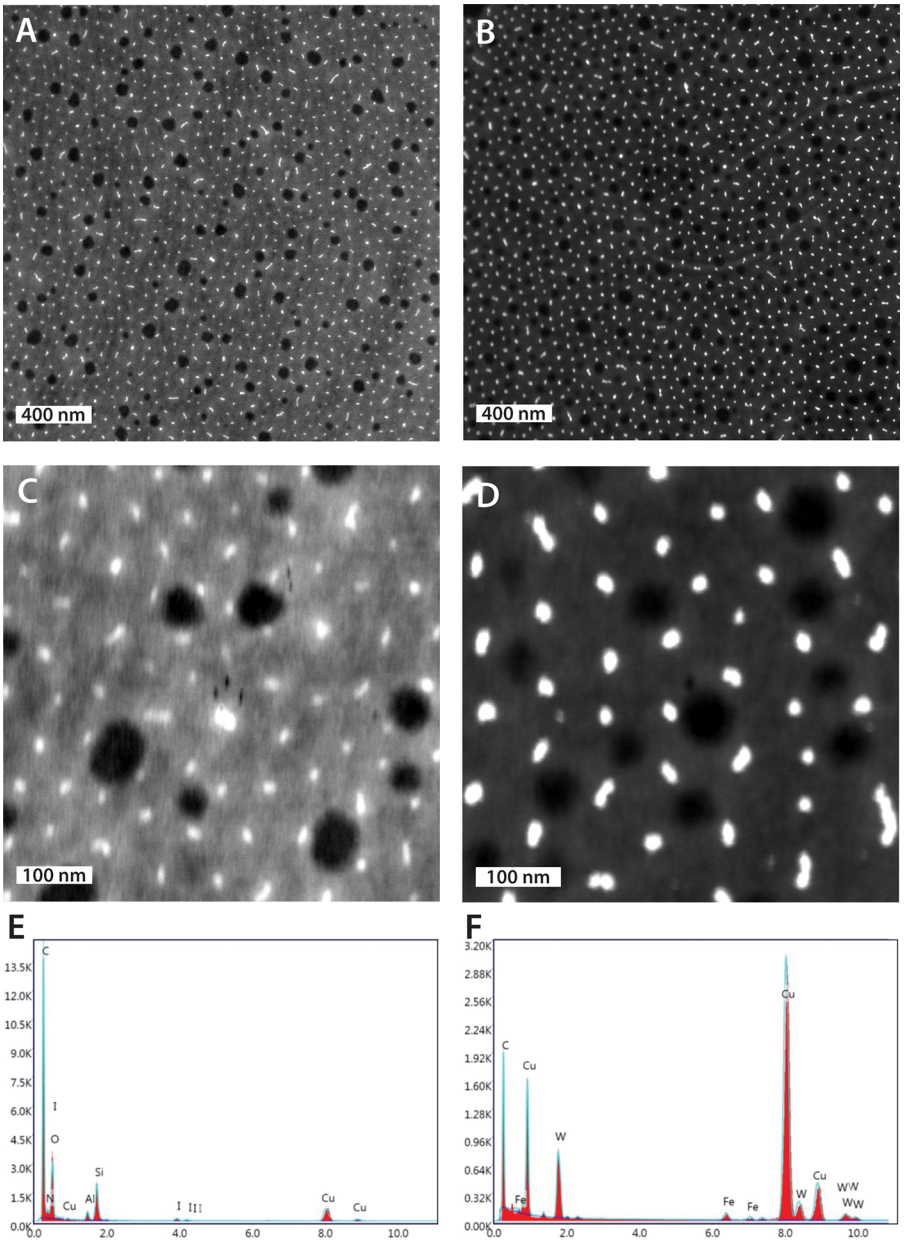

Figure 2. HAADF-STEM images of the (A and C) polymer and (B and D) polymer/$Fe_{30}W_{72}$ samples. The scale bars in panels A and B represent 400 nm, and the scale bars in panels C and D represent 100 nm. EDAX spectra of associated images and compositional information displayed for the (E) polymer and (F) polymer/$Fe_{30}W_{72}$ samples.

such depositions. For example, POM catalytic activity[33,34] and selectivity[35,36] can be affected by depositing POMs at interfaces.

POMs are of interest in magnetic applications due to their magnetic diversity, owing to their ability to host delocalized electrons and their aptitude for encapsulating clusters of magnetic transition metal centers.[37] While POMs are generally paramagnetic in nature, intramolecular electronic coupling in some POMs has demonstrated antiferromagnetic and ferromagnetic interactions.[22] Some POMs even demonstrate single-molecule magnetic behavior.[38,39] It is in light of these characteristics that POMs have potential for applications in modern computing technology.[40]

Herein, we combine the structuring abilities of block copolymers with the magnetic properties of POMs to create ordered films of magnetic clusters on magnetic substrates, toward bottom-up fabricated magnonic crystals. We fabricate a composite material utilizing a block copolymer of poly(styrene-*b*-4-vinylpyridine methyl iodide) (PS-*b*-P4VP) to form an ordered matrix of micelles, into which the iron tungstate POM, $Fe_{30}W_{72}$, is bound. The aim of this work was to establish a method for producing these organized films and understanding the magnetic implications of such hierarchical organization of POMs. The composite films were produced on both nonmagnetic silicon wafers and silicon wafers with a magnetic permalloy coating and characterized by imaging, polarized neutron reflectometry (PNR), and magnetization measurements. The results reveal that this is a viable fabrication approach for the bottom-up fabrication of magnonic crystals.

For this work, an iron- and tungsten-containing POM was selected due to its known magnetic properties.[41,42] It has a

https://doi.org/10.1021/acs.nanolett.3c03825
Nano Lett. 2024, 24, 2165−2174

structural formula of $Na_6(NH_4)_{20}(Fe(H_2O)_6)_2[\{(W)W_5O_{21}(SO_4)\}_{12}\{(Fe(H_2O))_{30}\}(SO_4)_{13}(H2O)_{34}]$, abbreviated as $Fe_{30}W_{72}$, and belongs to the subclass of Keplerates, with a general formula of $\{(M)M_5\}_{12}(linker)_{30}$ (M = Mo, W, Cr, or V), which in this case consists of 12 pentagonal units of tungsten located at the vertices of an icosahedron that are linked through 30 Fe^{3+} centers. Linkers in the form of 20 NH_4^+ ions hold the molecule together in a crown ether type structure that is ~2.5 nm in diameter.[41] $Fe_{30}W_{72}$ is visually represented in Figure 1A. We have previously synthesized and characterized this POM[41] and here add further magnetic susceptibility measurements. Infrared spectra and the corresponding mode assignment are available in Figure S1. The nuclear magnetic resonance (NMR)-based Evans method[43] was applied to calculate an average effective magnetic moment (μ_{eff}) of 19 μ_B (details in the Supporting Information). Figure 1B shows the molar magnetic susceptibility as a function of temperature (and χ_{mol}^{-1} in the inset of Figure 1B) obtained using SQUID magnetometry, clearly demonstrating the paramagnetism of $Fe_{30}W_{72}$. Plotting the data as $\chi_{mol}T$ emphasizes the type of magnetism observed in the molecule. For a perfect paramagnet, $\chi_{mol}T$ would be constant with respect to temperature. Here, $\chi_{mol}T$ shows a gradual decrease as the temperature decreases, followed by a large decrease in $\chi_{mol}T$ below ~50 K, indicating that $Fe_{30}W_{72}$ deviates from a perfect paramagnet. To add to this, a graph of χ_{mol}^{-1} versus T was generated (Figure 1B, inset) and the Curie−Weiss temperature was found to be −14 K. The decrease in $\chi_{mol}T$ at low temperatures and the negative Curie−Weiss temperature indicate that there is antiferromagnetic coupling[44] between magnetic moments within the molecule, which in this case has been previously shown to be due to the Fe^{III} centers.[45] The presence of antiferromagnetic coupling provides a mechanism by which the POMs may couple to nearby magnetic objects and modify their properties. We will next demonstrate nanoscale templating of the POMs using a copolymer templating method and then investigate the effect of the POM template on the magnetic properties of an underlying permalloy layer.

We have previously incorporated ligand-functionalized hydrophobic $Fe_{30}W_{72}$ POMs into the corona of block copolymer micelles.[41] For the purpose of creating an ordered magnonic structure, it is preferable to load magnetic cargo into the core of the micelles. To do so, block copolymer PS-*b*-P4VP was selected [Fourier transform infrared (FT-IR) data available in Figure S3], where the positively charged block can undergo an ion exchange reaction with the POMs, displacing the iodide and binding the POMs.[46] In our method, micelles were first deposited "bare" on substrates and subsequently exposed to an aqueous solution containing POMs. The water is assumed to open up the micelles to allow POM to selectively bind to the pyridinium core. Similar approaches have been used to bind salts of gold,[47] iron,[48] and others.[49−51] Panels C, F, and I of Figure 1 show atomic force microscopy (AFM) images of the micelles as spin-coated onto the silicon wafers, while the middle column is after exposure to water and the right column is after binding of the POMs to the polymer. From the height profiles (Figure 1C−H), the micelles are seen to form a semiordered array, with the micelle cores being visible in the AFM image as elevated spots surrounded by a relatively continuous layer of the lower hydrophobic polystyrene coronas. A line scan taken across the image shows an average height of these micelles of ~9 nm and an average center-to-center distance of 82 ± 6 nm. For comparison, AFM was also performed on micelles deposited on permalloy-coated silicon wafers (Figure S4), showing similar organization despite a rougher underlying substrate.

Figure 1 also demonstrates that the structural integrity of the micelle film is maintained upon exposure to both water (middle column) and $Fe_{30}W_{72}$ (right column). After exposure to either pure water or an $Fe_{30}W_{72}$ solution, there is a slight expansion of the micelle core. Upon exposure to water, the micelles open up to reveal the P4VP, as seen in similar polymer systems,[52] corroborated by the phase images. Upon exposure to water, the micelle cores display a phase value much lower than that of the surrounding matrix, consistent with the stiffer P4VP block being exposed.[53,54]

Scanning tunneling electron microscopy (STEM) with energy dispersive X-ray analysis (EDAX) was used to confirm the binding of POM to the micelle core. Figure 2A−D shows the HAADF-STEM images of the polymer and polymer/$Fe_{30}W_{72}$ films. Dark-field imaging means that atoms with a higher electron density show up as brighter spots. Even before the binding of $Fe_{30}W_{72}$ to the micelles, the micelle cores are brighter than the surrounding corona (Figure 2A,C), which is attributed to the relatively heavy element iodine, which is complexed into the P4VP cores. After $Fe_{30}W_{72}$ exposure (Figure 2B,D), it is clear, by the increased contrast difference, that the distribution of electron density has changed dramatically. This is attributed to the heavy element-containing and electron-dense $Fe_{30}W_{72}$ POMs now residing in the cores of the micelles. This selective binding of the POMs to the P4VP is consistent with the ability of the POMs to undergo an ionic exchange reaction with iodine, as observed previously in the functionalization of POMs with didodecylammonium bromide.[41] The average center-to-center distance between the micelles from the transmission electron microscopy (TEM) images was measured with ImageJ to be 86 ± 4 nm, in agreement with the AFM data.

The EDAX spectrum from the micelle core of the polymer/$Fe_{30}W_{72}$ sample (Figure 2F) confirms the presence of tungsten and iron, not present before POM binding (Figure 2E). The areas between the bright spots (Figure S4) do not contain any tungsten, iron, or iodine. Copper is attributed exclusively to the TEM grid. This data make it clear that the $Fe_{30}W_{72}$ POMs have indeed made it into the micelle cores. The atomic percentages generated from the EDAX spectra (Figure S5) show a ratio of ~1.6:1 tungsten atoms to iron atoms. The discrepancy from the theoretical ratio of 2.3:1 can be attributed to uncertainties in fitting a baseline to the EDAX spectra, especially for these elements that are present in small amounts. In the next section, we will explore how the organized POMs affect the magnetic properties of an underlying magnetic thin film. The STEM images and EDAX data demonstrate that the POMs bind to the micelle cores, but we have not attempted to tailor the POM loading.

PNR is a technique capable of measuring depth-resolved magnetization. PNR was used to investigate the magnetic structure in the following samples at 300 and 10 K: silicon wafers with a polymer layer (Si-micelle), silicon wafers with a permalloy coating and polymer layer (Si-NiFe-micelle), silicon wafers with a polymer/$Fe_{30}W_{72}$ layer [Si-micelle($Fe_{30}W_{72}$)], and silicon wafers with a permalloy coating and polymer/$Fe_{30}W_{72}$ layer [Si-NiFe-micelle($Fe_{30}W_{72}$)]. The models from the collected data were built systematically by first fitting and modeling the permalloy and micelle layers (Figure 3), followed

https://doi.org/10.1021/acs.nanolett.3c03825
Nano Lett. 2024, 24, 2165−2174

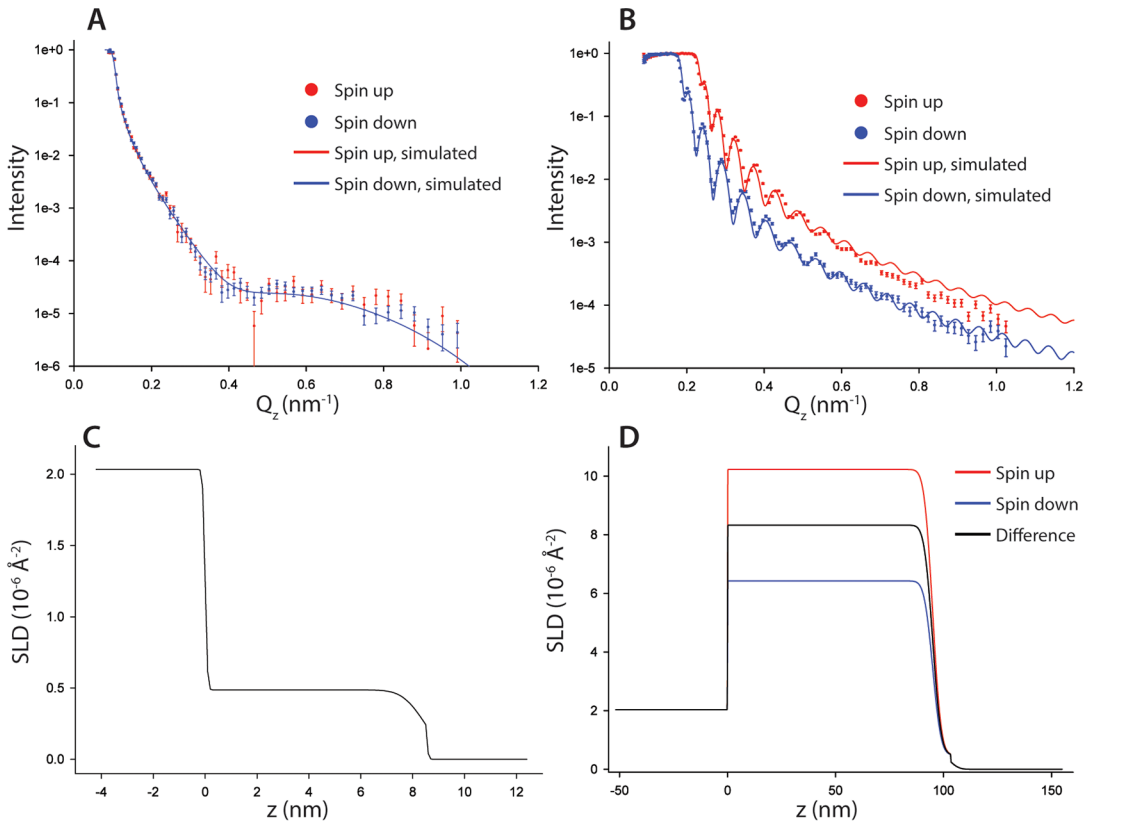

Layer	Thickness (nm)	SLD (10^{-6} Å^{-2})	Roughness	Magnetization (μ_B)
Substrate	0	2.03	0.1	0
Micelle	8.5	0.48	1	0
Vacuum	0	0	0	0

Layer	Thickness (nm)	SLD (10^{-6} Å^{-2})	Roughness	Magnetization (μ_B)
Substrate	0	2.03	0.1	0
NiFe	95	8.33	4.34	0.8
Micelle	8.5	0.48	0.1	0
Vacuum	0	0	0	0

Figure 3. (A and B) PNR reflected spectra and (C and D) corresponding SLD profiles of the Si-micelle at 10 K (left) and the Si-NiFe-micelle at 10 K (right), respectively, with associated fitting parameters. The parameter z is the distance from the surface of the Si substrate. In panel C, z = 0−8.5 nm is thus the micelle layer, while in panel D, z = 1−95 nm is the permalloy layer.

by the fitting of the added POM layer (Figure 4). The resulting model then allows investigation of the effect of the polymer/POM film on the magnetic properties of the underlying permalloy substrate (Figure 5).

Information from the AFM and TEM images was used to determine the correct model for the simulation. As expected, there was no detectable magnetism in the Si-micelle sample [no splitting of the spin-up and spin-down signals (Figure 3A)]. The scattering length density (SLD) of the polymer layer is ∼0.5×10^{-6} Å^{-2} (Figure 3C). A uniform polystyrene surface would have an expected value of 1.4×10^{-6} Å^{-2}.[55] This is attributed to the structure of the micellar film, with peaks and troughs of ∼9 nm. The simulation parameters suggest that the polymer layer has approximate volume fraction of 35%.

The parameters of the Si-micelle model (Figure 3A,C) were used as a base to model the profile for the Si-NiFe-micelle (Figure 3B,D). The parameters for the micelle layer and substrate (silicon wafer) were fixed, but the addition of the permalloy layer between these two accounted for the differences seen between the two reflection patterns in panels A and C of Figure 3. One of the most prominent features of the permalloy-reflected pattern is the large splitting between the spin-up and spin-down reflection signals. This signifies that the permalloy has a strong net magnetic moment. The net magnetization of the permalloy layer was fitted to be 0.8 μ_B per atom, consistent with past permalloy films that have 0.7−1.0 μ_B per atom (corresponding to 600−800 emu/cm^3).[56,57] A thickness of 97 nm was extrapolated from the Kiessig fringe spacing in the spectra. The chemical/nuclear SLD of the permalloy is ∼8.33×10^{-6} Å^{-2}, which is expected of a $Ni_{80}Fe_{20}$ permalloy film.[58] These models were used as a baseline for the analysis of the remaining samples.

Figure 4 shows the Si-micelle($Fe_{30}W_{72}$) sample measured at 300 and 10 K. Many different models were attempted to accurately fit the spectra, including single-layer and multiple-layer models. The best fitting model for a single layer can be found in Figure S6. It was found that the best fit was obtained when the polymer/POM layer atop the surface was treated as two layers. The first layer consists of a 3.5 nm polystyrene layer. The second, top, layer is a polymer/POM combined layer, modeled to be 3 nm thick with an SLD representing an average of the POMs and the polymer. This suggests that the POMs place themselves only in the top layer of the micelles and on average reach down no further than 3 nm into the micelles. This agrees with the result from TEM/EDAX, which demonstrated that the POMs reside in the 4PVP cores of the micelles and are excluded from the polystyrene corona, which wets the substrate. The new average SLD also gives an estimate of the POM loading within that top polymer layer of 20 atom

https://doi.org/10.1021/acs.nanolett.3c03825
Nano Lett. 2024, 24, 2165−2174

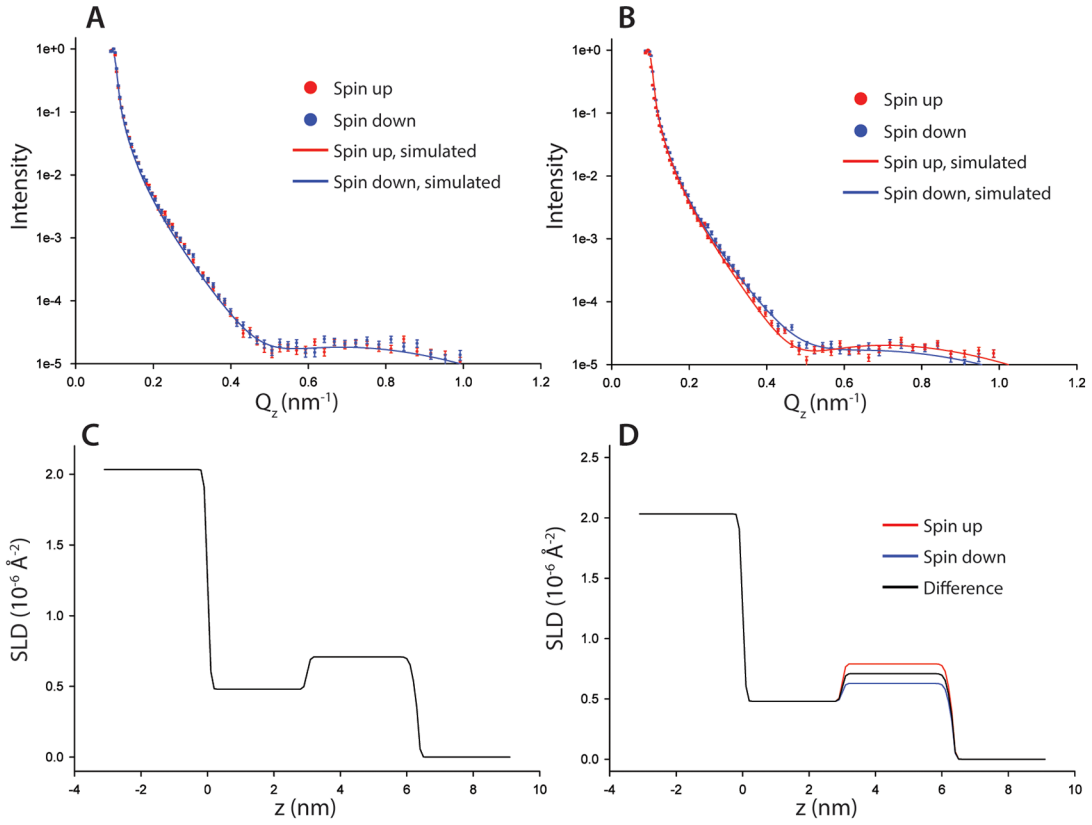

Layer	Thickness (nm)	SLD (10^{-6} Å^{-2})	Roughness	Magnetization (μ_B)
Substrate	0	2.03	0.1	0
Micelle	2.97	0.48	0.1	0
$Fe_{30}W_{72}$	3.26	0.71	0.2	0
Vacuum	0	0	0	0

Layer	Thickness (nm)	SLD (10^{-6} Å^{-2})	Roughness	Magnetization (μ_B)
Substrate	0	2.03	0.1	0
Micelle	2.97	0.48	0.1	0
$Fe_{30}W_{72}$	3.26	0.71	0.2	0.30
Vacuum	0	0	0	0

Figure 4. (A and B) PNR reflected spectra and (C and D) corresponding SLD profiles of the Si-micelle($Fe_{30}W_{72}$) at 300 K (left) and the Si-micelle($Fe_{30}W_{72}$) at 10 K (right), respectively, with associated fitting parameters. The parameter z is the distance from the surface of the Si substrate.

% POM to polymer (assuming a POM SLD as calculated to be 1.5×10^{-6} Å^{-2}).

A splitting of the spin-up and spin-down signals in the reflection pattern of the Si-micelle($Fe_{30}W_{72}$) sample can be detected at 10 K (Figure 4B,D) (a best fit model based on zero splitting can be found in Figure S7). The model was kept entirely the same as at 300 K, apart from the POM magnetization, found to be 0.3 μ_B per 10^{-28} m^3. This lines up well with the magnetic data gathered from SQUID magnetometry that show there is a clear increase in the magnetic susceptibility of the POM with a decrease in temperature.

The PNR data for the sample deposited on permalloy-coated Si [Si-NiFe-micelle($Fe_{30}W_{72}$)] were fit in Figure 5. The permalloy layer is situated between the silicon substrate and the micelle layer. The fitting of the reflection pattern taken at 300 K used identical parameter constraints with respect to the permalloy layer in Figure 3, and the same parameters for the micelles were also used as per Figure 4 for the Si-micelle($Fe_{30}W_{72}$) at 300 K.

The difference between the SLD profiles in panels C and D of Figure 5 is not easily seen, as the splitting due to the permalloy layer is large compared to the splitting caused by the POMs in the polymer/$Fe_{30}W_{72}$ layer. Upon careful examination, one can see that the splitting between the spin-up and spin-down data is smaller at 10 K (Figure 5D) than at 300 K (Figure 5C). In fact, the magnetization of the permalloy must be reduced by ~0.15 μ_B to fit (a simulated fit with no reduction in magnetism can be found in Figure S8), suggesting that the presence of POMs on the permalloy surface is causing a decrease in the magnetization of the permalloy layer. Magnetization measurements on the same sample, in Figures S9 and S10, confirm the net magnetization decrease. Importantly, there is no decrease in magnetization seen in the PNR of the permalloy-coated silicon wafer alone (Figures S11 and S12). The decrease in the net magnetization occurs for only samples coated with POMs and may imply that the POM magnetization is antiferromagnetically aligned to the permalloy at low temperatures. Figures S12 and S13 show a model that considers the possibility of a complex interfacial profile in which the POM is antiferromagnetically aligned to the permalloy surface. Although this model also describes the data well, there is considerable statistical uncertainty in determining the magnitude and direction of the POM layer, as the permalloy is the main contributor to the magnetic signal and the fits with or without the POM layer magnetization are very similar (Figure S12).

Taken together, the PNR results demonstrate that the magnitude of the neutron spin asymmetry (whereby the permalloy films split the signals from the spin-up and spin-

https://doi.org/10.1021/acs.nanolett.3c03825
Nano Lett. 2024, 24, 2165−2174

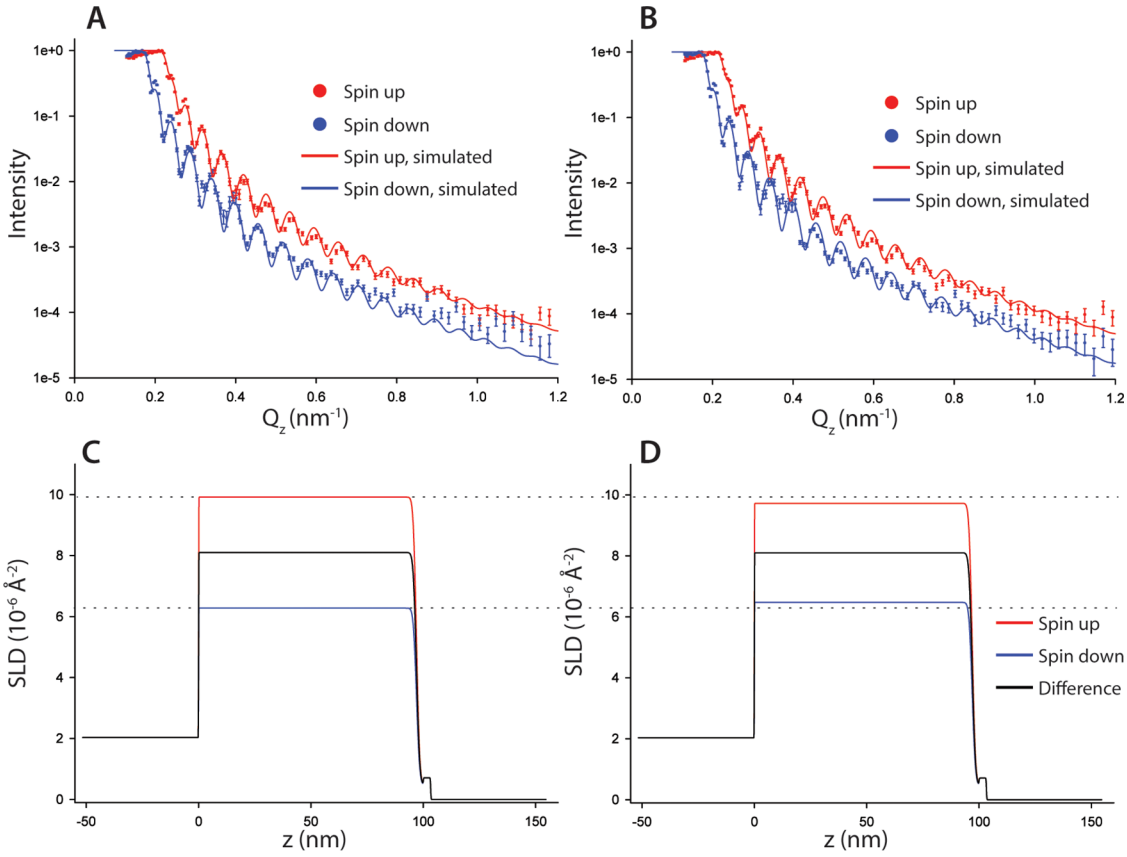

Layer	Thickness (nm)	SLD (10^{-6} Å^{-2})	Roughness	Magnetization (μ_B)
Substrate	0	2.03	0.1	0
NiFe	97	8.1	1.6	0.8
Micelle	2.97	0.48	0.1	0
$Fe_{30}W_{72}$	3.26	0.71	0.2	0
Vacuum	0	0	0	0

Layer	Thickness (nm)	SLD (10^{-6} Å^{-2})	Roughness	Magnetization (μ_B)
Substrate	0	2.03	0.1	0
NiFe	97	8.1	1.6	0.65
Micelle	2.97	0.48	0.1	0
$Fe_{30}W_{72}$	3.26	0.71	0.2	0.30
Vacuum	0	0	0	0

Figure 5. (A and B) PNR reflected spectra and (C and D) corresponding SLD profiles of the Si-NiFe-micelle($Fe_{30}W_{72}$) at 300 K and the Si-NiFe-Micelle($Fe_{30}W_{72}$) at 10 K, respectively, with associated fitting parameters. The parameter z is the distance from the surface of the Si substrate.

down reflection pattern) is not affected by a polymer or polymer/$Fe_{30}W_{72}$ layer at 300 K. When the polymer/$Fe_{30}W_{72}$ layer is present on top of the permalloy, however, the low-temperature magnetization of the permalloy layer and the spin asymmetry are reduced, which can be observed only at 10 K.

It is surprising that such a thin layer of weakly magnetic POMs can cause an observable shift in the magnetization of a relatively thick layer of permalloy, yet the PNR data and modeling, together with complementary magnetometry measurements, show that this is the case. We propose that this is caused by a type of exchange bias in which the antiferromagnetic nature of the $Fe_{30}W_{72}$ POMs couples with the magnetic moments of the permalloy and thus inhibits some of the permalloy film from reaching full magnetic alignment in the applied field. An apparent exchange bias is present also in the magnetization measurements of Figure S9. Further investigation is required to fully understand this observed feature.

Exchange bias is an interfacial phenomenon, of interest in applications such as magnetic recording media and spin-wave sensors.[59,60] Exchange bias has been most commonly described for layered antiferromagnetic/ferromagnetic structures such as cobalt and its native antiferromagnetic oxide. In such configurations, the antiferromagnetic layer has been demonstrated to pin the interfacial spins of a soft ferromagnet. Exchange bias has also been demonstrated for molecular organic systems.[61,62] There is still much left to learn about the exchange bias phenomenon in general and about exchange bias in molecular systems in particular. Recent work by Avedissian et al.[63] suggested that several published molecular exchange bias effects are instead uncontrolled oxidation of the underlying ferromagnetic film. While we cannot fully rule out such effects in the system presented here, it is important to note two things. First, the reduction in permalloy magnetization is not seen for the sample with micelles alone. As the samples are the same age and from the same permalloy-coated wafer, that tells us that it is not a simple oxidation in air or from processing conditions. Second, for the sample with POM-containing micelles on the permalloy, the effect on the underlying permalloy film is seen at only 10 K and not 300 K. Taken together, this indicates that the effect is not as simple as destroying, oxidizing, or etching the permalloy film. Our data suggest that the POMs are separated from the permalloy by a polymer layer, so it is also unlikely to be a direct oxidation of the surface by the POMs. It is clear from the literature that systems that enable tunability and controlled order/disorder of the antiferromagnetic layer are of particular interest for designing spinterfaces and exchange bias systems.[64]

https://doi.org/10.1021/acs.nanolett.3c03825
Nano Lett. 2024, 24, 2165−2174

The results presented in this work highlight POMs as promising candidates for producing patterned magnetic substrates, and the micelle templating method offers options for creating patterns of POMs at a variety of interfaces. Patterning of POMs, beyond simple deposition, has been attempted previously,[65−69] including using block copolymers.[41,46,51,70−72] Previous approaches, however, have incorporated POMs into the polymer in solution prior to BCP assembly at an interface. Such approaches often see effects on the BCP order and structure as a function of an increasing level of POM incorporation. The method presented here avoids those effects. Thus, the POM patterning method presented here, and the observed exchange bias, offers potential for future development of hybrid materials incorporating POMs, with applications for magnonics and beyond, for example, in neuromorphic computing[73] and magneto optically coupled devices.

■ ASSOCIATED CONTENT

Supporting Information

The Supporting Information is available free of charge at https://pubs.acs.org/doi/10.1021/acs.nanolett.3c03825.

Materials and Methods and FT-IR spectra of the POM and polymer, details of Evan's method (including NMR spectra), images of micelles deposited on the permalloy, additional TEM with EDAX data, several alternative PNR models, and magnetization measurements (PDF)

■ AUTHOR INFORMATION

Corresponding Author

Jenny Malmström − *Department of Chemical and Materials Engineering, University of Auckland, Auckland 1010, New Zealand; The MacDiarmid Institute for Advanced Materials and Nanotechnology, Wellington 6012, New Zealand;* orcid.org/0000-0003-1473-0947; Email: j.malmstrom@auckland.ac.nz

Authors

Daniel R. M. Clyde − *Department of Chemical and Materials Engineering, University of Auckland, Auckland 1010, New Zealand; School of Chemical Sciences, University of Auckland, Auckland 1010, New Zealand; The MacDiarmid Institute for Advanced Materials and Nanotechnology, Wellington 6012, New Zealand*

David L. Cortie − *Australian Nuclear Science and Technology Organisation, Lucas Heights, NSW 2234, Australia;* orcid.org/0000-0003-2383-1619

Simon Granville − *The MacDiarmid Institute for Advanced Materials and Nanotechnology, Wellington 6012, New Zealand; Robinson Research Institute, Victoria University of Wellington, Wellington 6012, New Zealand*

David C. Ware − *School of Chemical Sciences, University of Auckland, Auckland 1010, New Zealand*

Penelope J. Brothers − *Research School of Chemistry, Australian National University, Canberra, ACT 2600, Australia;* orcid.org/0000-0001-8350-2361

Complete contact information is available at: https://pubs.acs.org/10.1021/acs.nanolett.3c03825

Author Contributions

D.C.: methodology, investigation, preparation of the original draft, and visualization. D.L.C.: methodology, investigation, and reviewing and editing. S.G.: conceptualizaton, methodology, investigation, and reviewing and editing. D.C.W.: methodology, supervision, and reviewing and editing. P.J.B.: methodology, supervision, reviewing and editing, and funding acquisition. J.M.: conceptualizaton, methodology, supervision, project administration, visualization, and reviewing and editing.

Notes

The authors declare no competing financial interest.

■ ACKNOWLEDGMENTS

The MacDiarmid Institute for Advanced Materials and Nanotechnology and the University of Auckland are acknowledged for their support of this research and for providing a doctoral scholarship for D.C., respectively. The authors acknowledge the support of Dr. Adrian Turner and Joe Vella for their valuable inputs on TEM and AFM microscopy, Prof. Duncan McGillivray for discussions of neutron scattering, and Dr. Seong Nam for training in POM synthesis. The authors acknowledge the support of the Australian Nuclear Science and Technology Organisation for providing beam facilities for Polarized Neutron Reflectometry (P9785).

■ REFERENCES

(1) Bhat, W. A. Bridging data-capacity gap in big data storage. *Future Generation Computer Systems* **2018**, *87*, 538−548.

(2) Zhang, Y.; Zhao, Y.; Dai, S.; Nie, B.; Ma, H.; Li, J.; Miao, Q.; Jin, Y.; Tan, L.; Ding, Y. Cooling technologies for data centres and telecommunication base stations - A comprehensive review. *Journal of Cleaner Production* **2022**, *334*, 130280.

(3) Fulpagare, Y.; Bhargav, A. Advances in data center thermal management. *Renewable and Sustainable Energy Reviews* **2015**, *43*, 981−996.

(4) Kruglyak, V. V.; Demokritov, S. O.; Grundler, D. Magnonics. *J. Phys. D: Appl. Phys.* **2010**, *43* (26), 264001.

(5) Gomonay, O.; Jungwirth, T.; Sinova, J. Concepts of antiferromagnetic spintronics. *Phys. Status Solidi RRL* **2017**, *11* (4), 1700022.

(6) Kajiwara, Y.; Harii, K.; Takahashi, S.; Ohe, J.; Uchida, K.; Mizuguchi, M.; Umezawa, H.; Kawai, H.; Ando, K.; Takanashi, K.; Maekawa, S.; Saitoh, E. Transmission of electrical signals by spin-wave interconversion in a magnetic insulator. *Nature* **2010**, *464* (7286), 262−266.

(7) Bunyaev, S. A.; Golub, V. O.; Salyuk, O. Y.; Tartakovskaya, E. V.; Santos, N. M.; Timopheev, A. A.; Sobolev, N. A.; Serga, A. A.; Chumak, A. V.; Hillebrands, B.; Kakazei, G. N. Splitting of standing spin-wave modes in circular submicron ferromagnetic dot under axial symmetry violation. *Sci. Rep.* **2016**, *5*, 18480.

(8) Kim, S. K.; Lee, K. S.; Han, D. S. A gigahertz-range spin-wave filter composed of width-modulated nanostrip magnonic-crystal waveguides. *Appl. Phys. Lett.* **2009**, *95* (8), 082507.

(9) Chumak, A. V.; Serga, A. A.; Hillebrands, B.; Kostylev, M. P. Scattering of backward spin waves in a one-dimensional magnonic crystal. *Appl. Phys. Lett.* **2008**, *93* (2), 022508.

(10) Ding, J.; Adeyeye, A. O. Binary ferromagnetic nanostructures: Fabrication, static and dynamic properties. *Adv. Funct. Mater.* **2013**, *23* (13), 1684−1691.

(11) Sahoo, S.; Mondal, S.; Williams, G.; May, A.; Ladak, S.; Barman, A. Ultrafast magnetization dynamics in a nanoscale three-dimensional cobalt tetrapod structure. *Nanoscale* **2018**, *10* (21), 9981−9986.

(12) Yu, H.; D'Allivy Kelly, O.; Cros, V.; Bernard, R.; Bortolotti, P.; Anane, A.; Brandl, F.; Heimbach, F.; Grundler, D. Approaching soft X-ray wavelengths in nanomagnet-based microwave technology. *Nat. Commun.* **2016**, *7*, 11255.

(13) Barman, A.; Gubbiotti, G.; Ladak, S.; Adeyeye, A. O.; Krawczyk, M.; Grafe, J.; Adelmann, C.; Cotofana, S.; Naeemi, A.;

Vasyuchka, V. I.; Hillebrands, B.; Nikitov, S. A.; Yu, H.; Grundler, D.; Sadovnikov, A. V.; Grachev, A. A.; Sheshukova, S. E.; Duquesne, J. Y.; Marangolo, M.; Csaba, G.; Porod, W.; Demidov, V. E.; Urazhdin, S.; Demokritov, S. O.; Albisetti, E.; Petti, D.; Bertacco, R.; Schultheiss, H.; Kruglyak, V. V.; Poimanov, V. D.; Sahoo, S.; Sinha, J.; Yang, H.; Münzenberg, M.; Moriyama, T.; Mizukami, S.; Landeros, P.; Gallardo, R. A.; Carlotti, G.; Kim, J. V.; Stamps, R. L.; Camley, R. E.; Rana, B.; Otani, Y.; Yu, W.; Yu, T.; Bauer, G. E. W.; Back, C.; Uhrig, G. S.; Dobrovolskiy, O. V.; Budinska, B.; Qin, H.; Van Dijken, S.; Chumak, A. V.; Khitun, A.; Nikonov, D. E.; Young, I. A.; Zingsem, B. W.; Winklhofer, M. The 2021 Magnonics Roadmap. *J. Phys.: Condens. Matter* **2021**, *33* (41), 413001.

(14) Lan, J.; Yu, W.; Xiao, J. Antiferromagnetic domain wall as spin wave polarizer and retarder. *Nat. Commun.* **2017**, *8* (1), 178.

(15) Wang, X.; Goswami, M.; Kumar, R.; Sumpter, B. G.; Mays, J. Morphologies of block copolymers composed of charged and neutral blocks. *Soft Matter* **2012**, *8* (11), 3036−3052.

(16) Haryono, A.; Binder, W. H. Controlled arrangement of nanoparticle arrays in block-copolymer domains. *Small* **2006**, *2* (5), 600−611.

(17) Jang, S. G.; Kramer, E. J.; Hawker, C. J. Controlled supramolecular assembly of micelle-like gold nanoparticles in PS-b-P2VP diblock copolymers via hydrogen bonding. *J. Am. Chem. Soc.* **2011**, *133* (42), 16986−16996.

(18) Thompson, R. B.; Ginzburg, V. V.; Matsen, M. W.; Balazs, A. C. Block copolymer-directed assembly of nanoparticles: Forming mesoscopically ordered hybrid materials. *Macromolecules* **2002**, *35* (3), 1060−1071.

(19) Yao, Y.; Metwalli, E.; Su, B.; Körstgens, V.; Moseguí González, D.; Miasnikova, A.; Laschewsky, A.; Opel, M.; Santoro, G.; Roth, S. V.; Müller-Buschbaum, P. Arrangement of Maghemite Nanoparticles via Wet Chemical Self-Assembly in PS- b -PNIPAM Diblock Copolymer Films. *ACS Appl. Mater. Interfaces* **2015**, *7* (23), 13080−13091.

(20) Song, D. P.; Li, C.; Li, W.; Watkins, J. J. Block copolymer nanocomposites with high refractive index contrast for one-step photonics. *ACS Nano* **2016**, *10* (1), 1216−1223.

(21) Song, D. P.; Shahin, S.; Xie, W.; Mehravar, S.; Liu, X.; Li, C.; Norwood, R. A.; Lee, J. H.; Watkins, J. J. Directed Assembly of Quantum Dots Using Brush Block Copolymers for Well-Ordered Nonlinear Optical Nanocomposites. *Macromolecules* **2016**, *49* (14), 5068−5075.

(22) Clemente-Juan, J. M.; Coronado, E.; Gaita-Ariño, A. Magnetic polyoxometalates: From molecular magnetism to molecular spintronics and quantum computing. *Chem. Soc. Rev.* **2012**, *41* (22), 7464−7478.

(23) Zhang, T.; Liu, S.; Kurth, D. G.; Faul, C. F. J. Organized nanostructured complexes of polyoxometalates and surfactants that exhibit photoluminescence and electrochromism. *Adv. Funct. Mater.* **2009**, *19* (4), 642−652.

(24) Liu, X. L.; Wang, Y. T.; Ng, C. T.; Wang, R.; Jing, G. Y.; Yi, J. B.; Yang, J.; Bay, B. H.; Yung, L. Y. L.; Fan, D. D.; Ding, J.; Fan, H. M. Coating Engineering of MnFe2O4 Nanoparticles with Superhigh T2 Relaxivity and Efficient Cellular Uptake for Highly Sensitive Magnetic Resonance Imaging. *Adv. Mater. Interfaces* **2014**, *1* (2), 1300069.

(25) Pöselt, E.; Kloust, H.; Tromsdorf, U.; Janschel, M.; Hahn, C.; Maßlo, C.; Weller, H. Relaxivity optimization of a pegylated iron-oxide-based negative magnetic resonance contrast agent for T 2-weighted spin-echo imaging. *ACS Nano* **2012**, *6* (2), 1619−1624.

(26) Pothayee, N.; Balasubramaniam, S.; Pothayee, N.; Jain, N.; Hu, N.; Lin, Y.; Davis, R. M.; Sriranganathan, N.; Koretsky, A. P.; Riffle, J. S. Magnetic nanoclusters with hydrophilic spacing for dual drug delivery and sensitive magnetic resonance imaging. *J. Mater. Chem. B* **2013**, *1* (8), 1142−1149.

(27) Zhao, J. W.; Li, Y. Z.; Chen, L. J.; Yang, G. Y. Research progress on polyoxometalate-based transition-metal-rare-earth heterometallic derived materials: Synthetic strategies, structural overview and functional applications. *Chem. Commun.* **2016**, *52* (24), 4418−4445.

(28) Casañ-Pastor, N.; Gómez-Romero, P. Polyoxometalates: From inorganic chemistry to materials science. *Front. Biosci.* **2004**, *9*, 1759−1770.

(29) Hill, C. L. Introduction: PolyoxometalatesMulticomponent Molecular Vehicles To Probe Fundamental Issues and Practical Problems. *Chem. Rev.* **1998**, *98* (1), 1−2.

(30) Long, D. L.; Burkholder, E.; Cronin, L. Polyoxometalate clusters, nanostructures and materials: From self assembly to designer materials and devices. *Chem. Soc. Rev.* **2007**, *36* (1), 105−121.

(31) Pope, M. T.; Müller, A. Polyoxometalate Chemistry: An Old Field with New Dimensions in Several Disciplines. *Angewandte Chemie International Edition in English* **1991**, *30* (1), 34−48.

(32) Cherevan, A. S.; Nandan, S. P.; Roger, I.; Liu, R.; Streb, C.; Eder, D. Polyoxometalates on Functional Substrates: Concepts, Synergies, and Future Perspectives. *Adv. Sci.* **2020**, *7* (8), 1903511.

(33) Inumaru, K.; Ishihara, T.; Kamiya, Y.; Okuhara, T.; Yamanaka, S. Water-Tolerant, Highly Active Solid Acid Catalysts Composed of the Keggin-Type Polyoxometalate H3PW12O40 Immobilized in Hydrophobic Nanospaces of Organomodified Mesoporous Silica. *Angew. Chem., Int. Ed.* **2007**, *46* (40), 7625−7628.

(34) Deshlahra, P.; Carr, R. T.; Chai, S.-H.; Iglesia, E. Mechanistic Details and Reactivity Descriptors in Oxidation and Acid Catalysis of Methanol. *ACS Catal.* **2015**, *5* (2), 666−682.

(35) Gholamyan, S.; Khoshnavazi, R.; Rostami, A.; Bahrami, L. Immobilized Sandwich-Type Polyoxometalates [Mn4(XW9O34)2]n-on Tb-Doped TiO2 Nanoparticles as Efficient and Selective Catalysts in the Oxidation of Sulfides and Alcohols. *Catal. Lett.* **2017**, *147* (1), 71−81.

(36) Hong, L.; Win, P.; Zhang, X.; Chen, W.; Miras, H. N.; Song, Y.-F. Covalent Immobilization of Polyoxotungstate on Alumina and Its Catalytic Generation of Sulfoxides. *Chem. - Eur. J.* **2016**, *22* (32), 11232−11238.

(37) Clemente-Juan, J. M.; Coronado, E.; Gaita-Ariño, A.; Giménez-Saiz, C.; Gudel, H. U.; Sieber, A.; Bircher, R.; Mutka, H. Magnetic polyoxometalates: Anisotropie exchange interactions in the Co 3II moiety of [(NaOH2)Co3(H 2O)(P2W15O56)2] 17. *Inorg. Chem.* **2005**, *44* (10), 3389−3395.

(38) Ako, A. M.; Hewitt, I. J.; Mereacre, V.; Clérac, R.; Wernsdorfer, W.; Anson, C. E.; Powell, A. K. A ferromagnetically coupled Mn19 aggregate with a record S = 83/2 ground spin state. *Angewandte Chemie - International Edition* **2006**, *45* (30), 4926−4929.

(39) Baniodeh, A.; Liang, Y.; Anson, C. E.; Magnani, N.; Powell, A. K.; Unterreiner, A. N.; Seyfferle, S.; Slota, M.; Dressel, M.; Bogani, L.; Goß, K. Unraveling the influence of lanthanide ions on intra-and inter-molecular electronic processes in Fe 10Ln10 nano-toruses. *Adv. Funct. Mater.* **2014**, *24* (40), 6280−6290.

(40) Baldoví, J. J.; Cardona-Serra, S.; Gaita-Ariño, A.; Coronado, E. Design of Magnetic Polyoxometalates for Molecular Spintronics and as Spin Qubits. *Adv. Inorg. Chem.* **2017**, *69*, 213−249.

(41) Manuguri, S.; van der Heijden, N. J.; Nam, S. J.; Narasimhan, B. N.; Wei, B.; Cabero Z, M. A.; Yu, H.; Granville, S.; McGillivray, D. J.; Brothers, P. J.; Williams, D. E.; Malmström, J. Polymer Micelle Directed Magnetic Cargo Assemblies Towards Spin-wave Manipulation. *Adv. Mater. Interfaces* **2021**, *8* (15), 2100455.

(42) Todea, A. M.; Merca, A.; Bögge, H.; Glaser, T.; Pigga, J. M.; Langston, M. L. K.; Liu, T.; Prozorov, R.; Luban, M.; Schröder, C.; Casey, W. H.; Müller, A. Porous capsules {(M)M5}12Fe30 III (M = MoVI, WVI): Sphere surface supramolecular chemistry with 20 ammonium ions, related solution properties, and tuning of magnetic exchange interactions. *Angewandte Chemie - International Edition* **2010**, *49* (3), 514−519.

(43) Schubert, E. M. Utilizing the evans method with a superconducting NMR spectrometer in the undergraduate laboratory. *Journol of Chemical Education* **1992**, *69* (1), 62.

(44) Mugiraneza, S.; Hallas, A. M. Tutorial: a beginner's guide to interpreting magnetic susceptibility data with the Curie-Weiss law. *Commun. Phys.* **2022**, *5* (1), 95.

(45) Müller, A.; Kögerler, P.; Dress, A. W. M. Giant metal-oxide-based spheres and their topology: From pentagonal building blocks to

https://doi.org/10.1021/acs.nanolett.3c03825
Nano Lett. 2024, 24, 2165−2174

keplerates and unusual spin systems. *Coord. Chem. Rev.* **2001**, *222* (1), 193−218.
(46) Bu, W.; Uchida, S.; Mizuno, N. Micelles and vesicles formed by polyoxometalate-block copolymer composites. *Angewandte Chemie - International Edition* **2009**, *48* (44), 8281−8284.
(47) Selvan, S. T.; Spatz, J. P.; Klok, H. A.; Möller, M. Gold-polypyrrole core-shell particles in diblock copolymer micelles. *Adv. Mater.* **1998**, *10* (2), 132−134.
(48) Ghoshal, T.; Maity, T.; Godsell, J. F.; Roy, S.; Morris, M. A. Large scale monodisperse hexagonal arrays of superparamagnetic iron oxides nanodots: A facile block copolymer inclusion method. *Adv. Mater.* **2012**, *24* (18), 2390−2397.
(49) He, Q.; Huang, H.; Zheng, X. Y.; Xiao, J.; Yu, B.; Kong, X. J.; Bu, W. Polymer-Encapsulated Lanthanide-Containing Clusters as Platforms for Fabricating Magnetic Soft Materials. *ACS Appl. Mater. Interfaces* **2018**, *10* (20), 16947−16951.
(50) Zhang, B. Q.; Chen, G. D.; Pan, C. Y.; Luan, B.; Hong, C. Y. Preparation, characterization, and thermal properties of polystyrene-block-quaternized poly(4-vinylpyridine)/montmorillonite nanocomposites. *J. Appl. Polym. Sci.* **2006**, *102* (2), 1950−1958.
(51) Zhou, J.; Hu, J.; Li, M.; Li, H.; Wang, W.; Liu, Y.; Winans, R. E.; Li, T.; Liu, T.; Yin, P. Hydrogen bonding directed co-assembly of polyoxometalates and polymers to core-shell nanoparticles. *Materials Chemistry Frontiers* **2018**, *2* (11), 2070−2075.
(52) Chaudhari, A.; Ghoshal, T.; Shaw, M. T.; Cummins, C.; Borah, D.; Holmes, J. D.; Morris, M. A. Formation of sub-7 nm feature size PS-b-P4VP block copolymer structures by solvent vapour process. *Proc. SPIE* **2014**, 905110.
(53) Malmström, J.; Wason, A.; Roache, F.; Yewdall, N. A.; Radjainia, M.; Wei, S.; Higgins, M. J.; Williams, D. E.; Gerrard, J. A.; Travas-Sejdic, J. Protein nanorings organized by poly(styrene-block-ethylene oxide) self-assembled thin films. *Nanoscale* **2015**, *7* (47), 19940−19948.
(54) Dai, L. L.; Granick, S. Linear shear viscoelasticity of confined, end-attached polymers in a near-theta solvent. *J. Polym. Sci., Part B: Polym. Phys.* **2005**, *43* (23), 3487−3496.
(55) Hellweg, T.; Dewhurst, C. D.; Eimer, W.; Kratz, K. PNIPAM-co-polystyrene core-shell microgels: Structure, swelling behavior, and crystallization. *Langmuir* **2004**, *20* (11), 4330−4335.
(56) Qader, M. A.; Vishina, A.; Yu, L.; Garcia, C.; Singh, R. K.; Rizzo, N. D.; Huang, M.; Chamberlin, R.; Belashchenko, K. D.; van Schilfgaarde, M.; Newman, N. The magnetic, electrical and structural properties of copper-permalloy alloys. *J. Magn. Magn. Mater.* **2017**, *442*, 45−52.
(57) Yan, H.; Omar, G. J.; Zhao, Z. T.; Zhi Shiuh, L.; Ariando, A. High-quality NiFe thin films on oxide/non-oxide platforms via pulsed laser deposition at room temperature. *arXiv* **2023**, DOI: 10.48550/arXiv.2304.00357.
(58) Cortie, D. L.; Ting, Y. W.; Chen, P. S.; Tan, X.; Lin, K. W.; Klose, F. Enhancement of the magnetic interfacial exchange energy at a specific interface in NiFe/CoO/Co trilayer thin films via ion-beam modification. *J. Appl. Phys.* **2014**, *115* (7), 073901.
(59) Mundlia, S.; Chaudhary, S.; Peri, L.; Bhardwaj, A.; Panda, J. J.; Sasmal, S.; Raman, K. V. Robust Monolayer Exchange-Bias Effect in Molecular Crane-Pulley Response at Magnetic Surface. *Physical Review Applied* **2020**, *14* (2), 024095.
(60) Nogués, J.; Schuller, I. K. Exchange bias. *J. Magn. Magn. Mater.* **1999**, *192* (2), 203−232.
(61) Jo, J.; Byun, J.; Oh, I.; Park, J.; Jin, M. J.; Min, B. C.; Lee, J.; Yoo, J. W. Molecular Tunability of Magnetic Exchange Bias and Asymmetrical Magnetotransport in Metalloporphyrin/Co Hybrid Bilayers. *ACS Nano* **2019**, *13* (1), 894−903.
(62) Gruber, M.; Ibrahim, F.; Boukari, S.; Isshiki, H.; Joly, L.; Peter, M.; Studniarek, M.; Da Costa, V.; Jabbar, H.; Davesne, V.; Halisdemir, U.; Chen, J.; Arabski, J.; Otero, E.; Choueikani, F.; Chen, K.; Ohresser, P.; Wulfhekel, W.; Scheurer, F.; Weber, W.; Alouani, M.; Beaurepaire, E.; Bowen, M. Exchange bias and room-temperature magnetic order in molecular layers. *Nat. Mater.* **2015**, *14* (10), 981−984.
(63) Avedissian, G.; Arabski, J.; Wytko, J. A.; Weiss, J.; Papaefthimiou, V.; Schmerber, G.; Rogez, G.; Beaurepaire, E.; Meny, C. Exchange bias at the organic/ferromagnet interface may not be a spinterface effect. *Appl. Phys. Rev.* **2022**, *9* (1), 011417.
(64) Bergenti, I.; Dediu, V. Spinterface: A new platform for spintronics. *Nano Materials Science* **2019**, *1* (3), 149−155.
(65) Makinde, Z. O.; Van Der Heijden, N. J.; Clyde, D.; Nam, S.; Brothers, P. J.; Malmström, J.; Granville, S.; Domigan, L. J.; McGillivray, D. J.; Williams, D. E. Geometric Frustration and Long-Range Ordering Induced by Surface Pressure Oscillation in a Langmuir-Blodgett Monolayer of Magnetic Soft Spheres. *Langmuir* **2021**, *37* (33), 10150−10158.
(66) Wang, Y.; Hao, J. Inorganic-Organic Hybrid Materials Based on Nanopolyoxometalates. In *Supramolecular Chemistry of Biomimetic Systems*; Li, J., Ed.; Springer: Singapore, 2017; pp 355−394.
(67) Santoni, M.-P.; Hanan, G. S.; Hasenknopf, B. Covalent multi-component systems of polyoxometalates and metal complexes: Toward multi-functional organic-inorganic hybrids in molecular and material sciences. *Coord. Chem. Rev.* **2014**, *281*, 64−85.
(68) Lin, X.; Wang, Y.; Wu, L. Hexagonal Mesostructure and Its Disassembly into Nanofibers of a Diblock Molecule/Polyoxometalate Hybrid. *Langmuir* **2009**, *25* (11), 6081−6087.
(69) Li, B.; Li, W.; Li, H.; Wu, L. Ionic Complexes of Metal Oxide Clusters for Versatile Self-Assemblies. *Acc. Chem. Res.* **2017**, *50* (6), 1391−1399.
(70) Chai, S.; Cao, X.; Xu, F.; Zhai, L.; Qian, H. J.; Chen, Q.; Wu, L.; Li, H. Multiscale Self-Assembly of Mobile-Ligand Molecular Nanoparticles for Hierarchical Nanocomposites. *ACS Nano* **2019**, *13* (6), 7135−7145.
(71) Wang, G.; Li, J.; Shang, L.; He, H.; Cui, T.; Chai, S.; Zhao, C.; Wu, L.; Li, H. Nanostructured Polymer Composite Electrolytes with Self-Assembled Polyoxometalate Networks for Proton Conduction. *CCS Chemistry* **2022**, *4* (1), 151−161.
(72) Zhang, L.; Cui, T.; Cao, X.; Zhao, C.; Chen, Q.; Wu, L.; Li, H. Inorganic-Macroion-Induced Formation of Bicontinuous Block Copolymer Nanocomposites with Enhanced Conductivity and Modulus. *Angewandte Chemie - International Edition* **2017**, *56* (31), 9013−9017.
(73) Zhang, G.; Xiong, Z. Y.; Gong, Y.; Zhu, Z.; Lv, Z.; Wang, Y.; Yang, J. Q.; Xing, X.; Wang, Z. P.; Qin, J.; Zhou, Y.; Han, S. T. Polyoxometalate Accelerated Cationic Migration for Reservoir Computing. *Adv. Funct. Mater.* **2022**, *32* (45), 2204721.

https://doi.org/10.1021/acs.nanolett.3c03825
Nano Lett. 2024, 24, 2165−2174